Supporting Information

Colossal Room-Temperature Magnetoelectric Coupling in Anion-Deficient Layered Perovskite Films with Ordered Cation Distribution

Hongwei Wang,[1,2,†] Xiangfei Li,[3,†] Jun Miao,[1,2,†*] Kun Lin,[1] Qiang Li,[1] Xin Chen,[1] Yili Cao,[1] Xi Shen,[3] Youwen Long,[3] Yu Chen,[4] Jiaou Wang,[4] Jing Zhou,[5] Yi Wang,[6] Qiliang Li,[7] Richeng Yu,[3,*] Xianran Xing[1,*]

Affiliations:

[1] Institute of Solid State Chemistry, University of Science and Technology Beijing, Beijing 100083, China.

[2] School of Materials Science and Engineering, University of Science and Technology Beijing, Beijing 100083, China

[3] Beijing National Laboratory for Condensed Matter Physics, Institute of Physics, Chinese Academy of Sciences, Beijing 100190, China

[4] Institute of High Energy Physics, Chinese Academy of Sciences, Beijing 100049, China

[5] School of Materials Science and Engineering, Wuhan University of Technology, Wuhan 430070, China

[6] Key Laboratory of Material Modification by Laser, Ion and Electron Beams, Dalian University of Technology, Dalian 116024, China.

[7] Department of Advanced Manufacturing and Robotics, College of Engineering, Peking University, Beijing 100871, China

* Corresponding author. Email: J.miao@ustb.edu.cn; rcyu@iphy.ac.cn; xing@ustb.edu.cn;

† These authors contributed equally to this work

PFO ceramic target preparation

The $Pb_{2+1}Fe_2O_5$ ceramic target has been synthesized by solid-state reaction, where the proportion of PbO (Aladdin, America, 99.9%) to Fe_2O_3 (Aladdin, America, 99.9%) is 3: 1 because Pb volatilizes during the preparation of target and films. The powders were mixed by ball milling for 12 h, then sintered at 700 ℃ for 8h in air. The powder was then pressed into a pellet and sintered at 750 ℃ for 6 h in air.

The determination of average lattice parameters of $P_{1.24}$FO film (~ 46 nm)

The peak positions of STO substrate and $P_{1.24}$FO film can be extracted from RSM raw data using Gaussian fitting, which can further be used to calculate the pseudocubic lattice parameters of $P_{1.24}$FO film. The lattice parameters of tetragonal phase films can be calculated using the following formulas:

$$a_p = \frac{H_{sub}}{H_{film}} \times a_{sub} \quad (1)$$

$$c_p = \frac{L_{sub}}{L_{film}} \times c_{sub} \quad (2)$$

where a_p and c_p are in-plane and out-of-plane pseudocubic lattice parameters of $P_{1.24}$FO film, (H_{film}, L_{film}) and (H_{sub}, L_{sub}) are peak positions of $P_{1.24}$FO film and STO substrate obtained by Gaussian fitting (**Figures S1a** and **S1b**), a_{sub} and c_{sub} are in-plane and out-of-plane lattice parameters of STO substrate (3.905 Å). Therefore, we can further obtain the average lattice parameters of $P_{1.24}$FO film $a = a_p$ and $c = 9c_p$.[1] The results are shown in **Table S1**.

The ion radius of Pb^{2+} ions (1.19 Å) is larger than Fe^{3+} ions (0.645 Å), so Pb^{2+} ions occupying sites of Fe^{3+} ions will expand the crystal cell volume. Notably, despite the confinement of STO substrate and the presence of excessive Pb, which maintains the in-plane lattice parameter a

and increases the out-of-plane lattice parameter c, the emergence of dislocations with increasing thickness causes the $P_{1.24}FO$ unit cells to tilt. This tilting results in a slight increase in a and a decrease in c. Consequently, the average c of $P_{1.24}FO$ film is not as large as anticipated.

Calculation of the actual polarization value by the positive-up-negative-down (PUND) measurement

The actual ferroelectric polarization was measured by Positive-up-negative-down (PUND) measurements, which can separate switching currents from other contributions. Five triangular wave pulses are applied to the $P_{1.24}FO$ film as shown in **Figure S5a**. The preset pulse is used to pre-polarize the thin film in the same direction. Then, during the first positive voltage pulse, all active mechanisms will contribute to the measurement current I_P including leakage currents I_L, dielectric displacement current I_D, and ferroelectric displacement current I_F. Therefore, the current I_P:

$$I_P = I_F + I_D + I_L \tag{1}$$

Due to all dipoles have been switched during the second positive voltage pulse, only I_D and I_L contribute to the current I_U:

$$I_U = I_D + I_L \tag{2}$$

Thereby, the ferroelectric displacement current I_F will be obtained:

$$I_F = I_P - I_U \tag{3}$$

Further, the polarization value could be obtained by integrating the ferroelectric displacement current I_F with time:

$$P = \int I_F \, dt \tag{4}$$

Analysis of the causes of asymmetric polarization

We attribute the observed asymmetric polarization values to the presence of the built-in electric field. The origin of the built-in electric field is attributed to the asymmetric distribution of oxygen vacancies and the flexoelectric field.

For oxygen vacancies, as shown in **Figure S6**. We measured EELS mapping to analyze the distribution of O (red) and Fe (green) elements in $P_{1.24}FO$ film, and extracted the elements' single intensity along the out-of-plane direction. As shown in the profile of O element distribution, from the interface to the surface of $P_{1.24}FO$ film, the single intensity of O element gradually decreases, which indicates the content of O ions gradually decreases, meaning that oxygen vacancies mainly accumulate on one side of the surface. Oxygen vacancies originate from Pb^{2+} ions occupying Fe^{3+} ion sites. To maintain electrical neutrality, oxygen vacancies will be generated. The defect equation is as follows:

$$4PbO \xrightarrow{Pb_2Fe_2O_5} 2Pb_{Pb} + 2Pb'_{Fe} + 4O_O + V_O^{\cdot\cdot}$$

The signal intensity of Fe element progressively decreases from the interface to the surface, suggesting an increasing substitution of Fe sites by Pb from the interface to the surface. Therefore, oxygen vacancies mainly accumulate on one side of the surface. Furthermore, the oxygen vacancies with positive charges will generate a built electric field point from the surface (Pt) to the interface ($SrRuO_3$), resulting in the asymmetric *P-V* and *I-V* curves.

Due to the larger leakage current of PFO film, the dynamic P-E loop (**Figure 2b**) was obtained by the PUND method (**Figure S5a**). The PUND method calculates polarization by integrating displacement current over time, as described on page 2 of the Supporting

Information. Herein, we present a detailed introduction to the measurement process of the PUND method and how the built-in electric field affects the polarization. Notably, polarization current is generated during the reversal of ferroelectric domains, and the extent or number of these domain reversals directly influences the magnitude of polarization current.

The voltage sequence required for measuring polarization using the PUND method consists of "Preset", "Positive", "Up", "Negative" and "Down", as shown in **Figure S5a**. The "Preset" process involves applying a negative voltage to pre-polarize film and achieve upward polarization. The "Positive' process involves applying a positive voltage to switch ferroelectric domains and achieve downward polarization, where the generated current includes polarization displacement current, dielectric displacement current and leakage current. The "Up" process still involves applying a positive voltage, but the generated current only includes dielectric displacement current and leakage current. Therefore, the polarization displacement current resulting from ferroelectric domains switching is equal to the "Positive" process current minus the "Up" process current, as shown by the blue solid line in **Figure S5b**. Similarly, the upward polarization displacement current is equal to the "Negative" process current minus the "Down" process current, as shown by the orange solid line in **Figure S5b**. The polarization intensity can be obtained by integrating the current with time (**Figure 2b**). It can be seen that the polarization current in the positive voltage region is greater than that in the negative voltage region, therefore the polarization intensity in the positive voltage region is greater than that in the negative voltage region.

As shown in **Figure S5c**, the downward built-in electric field influences the pristine polarization state of the $P_{1.24}FO$ film, leading to a downward net polarization.[2,3] The "Preset"

process switches ferroelectric domains to upward polarization. Next, when a positive voltage is applied during the "Positive" process, the polarization direction of ferroelectric domains reverses downward. Due to the direction of the built-in electric field aligning with the external voltage, ferroelectric domains are easily reversed, resulting in a larger polarization current and therefore a larger polarization. When a negative voltage is applied during the "Negative" process, the opposing directions of the built-in electric field and the external electric field impede the upward reversal of ferroelectric domains, consequently leading to a reduced polarization current.

For flexoelectric field, as shown in **Figures S3c** and **S3d**. The gradient variation of in-plane strain along the thickness direction of the film will contribute to the out-of-plane polarization (P_{flexo})[4], which can be calculated by the following formula:

$$P_{flexo} = \mu \frac{\partial \varepsilon_{xx}}{\partial z}$$

where $\frac{\partial \varepsilon_{xx}}{\partial z}$ is the in-plane strain gradient along the thickness direction of the film. The flexoelectric coefficient μ can be estimated by the following formula:[5,6]

$$\mu \sim \chi \frac{e}{a}$$

Where χ is the dielectric susceptibility ($\chi = \varepsilon_r - 1 \approx \varepsilon_r$), e is the electron charge, and a is the in-plane lattice constant. The dielectric permittivity of $P_{1.24}FO$ film is 200 at 1 kHz measured by impedance analyzer (**Figure S13**). The average strain gradient is 3.82 × 10^5 m^{-1} of $P_{1.24}FO$ film determined by GPA. Consequently, the out-of-plane flexoelectric polarization is 0.32 μC/cm^2. Although the out-of-plane polarization induced by flexoelectricity is an order of magnitude lower than macroscopic polarization (~ 2 μC/cm^2), it remains a significant component of ferroelectric polarization.

The influence of different Pb/Fe ratios on ME coupling, ferroelectricity and magnetism.

Due to the volatility of Pb during the deposition of thin films, it is difficult to precisely control the Pb/Fe ratio of $P_{1.24}FO$ film. However, our Energy Dispersive Spectrometer (EDS) data of $P_{1.24}FO$ films with varying thicknesses revealed that the Pb/Fe ratio increases with film thickness (See **Figure S11**, **Table S4**), which is consistent with Fe *L*-edge signal intensity trend along thickness direction shown in **Figure S6**. **Figure S12a** indicates that the saturation magnetic moment increases with decreasing $P_{1.24}FO$ film thickness, which may be due to the increase in the relative content of Fe. We measured the ME coupling coefficients of PFO films where Pb/Fe ratio is about 1.05 ($P_{1.05}FO$) by SPM (**Figure S12b**), and compared them with the data (Pb/Fe ratio ~ 1.24, $P_{1.24}FO$) presented in **Figure 2h**. The ME coupling coefficients in different areas of $P_{1.05}FO$ film exhibit significant variation, which may be due to the uneven distribution of Pb/Fe ratio. The average ME coupling coefficient (~ 2.85×10^4 $mV \cdot cm^{-1} \cdot Oe^{-1}$) of $P_{1.05}FO$ film is lower than that of $P_{1.24}FO$ film (~ 5.35×10^4 $mV \cdot cm^{-1} \cdot Oe^{-1}$).

We compared the ferroelectric response for $P_{1.24}FO$ films and $P_{1.05}FO$ by PFM. As shown in **Figures S12c-f**, a higher Pb/Fe ratio results in a more pronounced phase reversal after applying box-in-box voltage, suggesting that excessive Pb is conducive to enhancing the ferroelectric response.

The antisite defect in $P_{1.24}FO$ film

Antisite defect is a very interesting phenomenon commonly observed in non-stoichiometric systems. Lee et al[7]. reported that the formation of polar nanoregions around Ti_{Sr} antisite defects

in Sr deficient $SrTiO_3$ film, and showed room-temperature ferroelectricity in thinner STO film. Gao et al.[8] reported that the Pb_{Zr} antisite defects are beneficial for the formation of ferroelectricity in $Pb_{1.2}ZrO_3$ film, rather than traditional anti-ferroelectricity ($PbZrO_3$). Ning et al.[9] reported that the presence of Y_{Fe} antisite defects facilitates a non-centrosymmetric distortion promoting ferroelectricity. In a word, the antisite defects can break the centrosymmetric structure and promote polarity distortion, which is beneficial for the formation and enhancement of ferroelectricity.

As shown in **Figure S9**, the Pb_{Fe} antisite defects in $P_{1.24}FO$ film can expand the c/a ratio within about 2 nm of the surrounding area, enhancing local polarity distortion, which is beneficial for achieving out-of-plane net polarization. Therefore, the ordered distribution of Pb/Fe ions in mixed layers and the Pb_{Fe} antisite defects in perovskite layers jointly contribute to the enhancement of out-of-plane polarization in $P_{1.24}FO$ film.

The influence of oxygen vacancies on ferroelectric switching

Oxygen vacancies are a double-edged sword. On the one hand, they can break spatial inversion symmetry producing ferroelectricity[10], even enhance ferroelectric polarization[11]. On the other hand, they can also pin ferroelectric domains increasing the coercive field[12], and affect ferroelectric stability[13]. The main reasons why oxygen vacancies affect ferroelectric stability are as follows:

1. **Generate leakage current**: Oxygen vacancies are equivalent to n-type doping, which introduces electrons into the materials and increases the leakage current.

2. **Increasing coercive field**: During ferroelectric switching, oxygen vacancy point defects can

hinder the growth and diffusion of ferroelectric domains, resulting in a high coercive field. Switching ferroelectric polarization at a higher voltage can deteriorate the ferroelectric cycle performance.[12]

3. **Producing dead layer**: During the ferroelectric switching process, oxygen vacancies will continuously accumulate at the electrode/ferroelectric layer interface, leading to a ferroelectric dead layer and rendering ferroelectric switching ineffective.[13]

The influence of SRO buffer layer on structure of $P_{1.24}FO$ film

Figure S14a shows the XRD patterns of Pt/$P_{1.24}$FO/SRO film and PFO film deposited on STO substrates. It can be observed that the characteristic peaks of PFO film deposited on the SRO bottom electrode exhibit a shift towards higher angles in comparison to that grown directly on STO, suggesting a decrease in the out-of-plane lattice constant. In addition, the originally weaker characteristic peaks of PFO (0 0 6), PFO (0 0 14), and PFO (0 0 20) disappeared directly on the $P_{1.24}FO$ film grown on the SRO bottom electrode, indicating its epitaxial quality was damaged. We measured RSM to determine the in-plane lattice parameters of $P_{1.24}FO$ film growing on the SRO bottom electrode, as shown in **Figure S14b**. The in-plane lattice parameter of $P_{1.24}FO$ film with SRO buffer layer is still the same as that of the STO substrate. **Table S1** shows the lattice parameters as well as the in-plane and out-of-plane strains of $P_{1.24}FO$ films, where the strains of $P_{1.24}FO$ films relative to the PFO bulk were calculated by the following formula:

$$\varepsilon_x = \frac{a_{film} - a_{bulk}}{a_{bulk}}$$

$$\varepsilon_y = \frac{c_{film} - c_{bulk}}{c_{bulk}}$$

Although the out-of-plane lattice parameter of $P_{1.24}FO$ film with SRO buffer layer are reduced compared to $P_{1.24}FO$ film grown on STO substrate, the out-of-plane lattice parameter of $P_{1.24}FO$ film with SRO buffer layer remains larger than that of PFO bulk. **Figure S14c** presents the HAADF image of $P_{1.24}FO$/SRO/STO, determining that the thickness of the SRO bottom electrode is 13 nm. Considering that the in-plane lattice parameter of PFO bulk is 3.905 Å and that of pseudocubic SRO is 3.923 Å[10], this stress mismatch may lead to damage to the $P_{1.24}FO$/SRO interface quality, resulting in ferroelectric performance degradation. **Figure S14d** shows the EELS mapping of Fe, Ru and Ti elements.

In summary, the c/a axis ratio of $P_{1.24}FO$ thin films deposited on the SRO bottom electrode diminishes due to damaged epitaxial quality, potentially inhibiting out-of-plane ferroelectricity, which is also consistent with the experimental polarization value being lower than theoretical polarization value (**Figure 4b**). In future studies, choosing an appropriate bottom electrode is a promising approach to improve epitaxial quality enhancing the ferroelectric polarization of PFO epitaxial thin films.

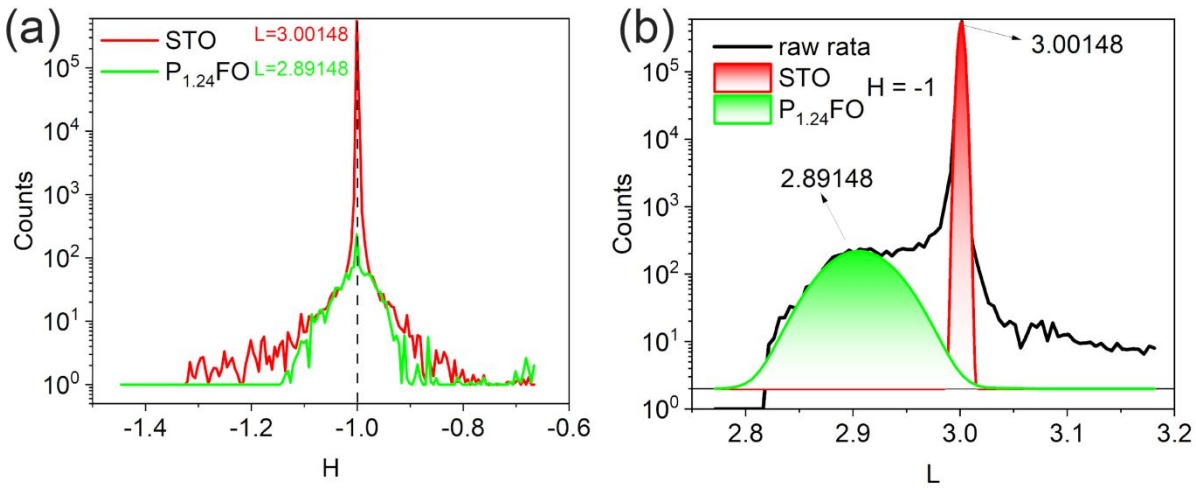

Figure S1. (a) The RSM intensity distribution of $P_{1.24}FO$ film and STO substrate at L = 2.89148 and L = 3.00148, respectively, varies with H. (b) The RSM intensity distribution of $P_{1.24}FO$ film and STO substrate at H = -1, varies with L.

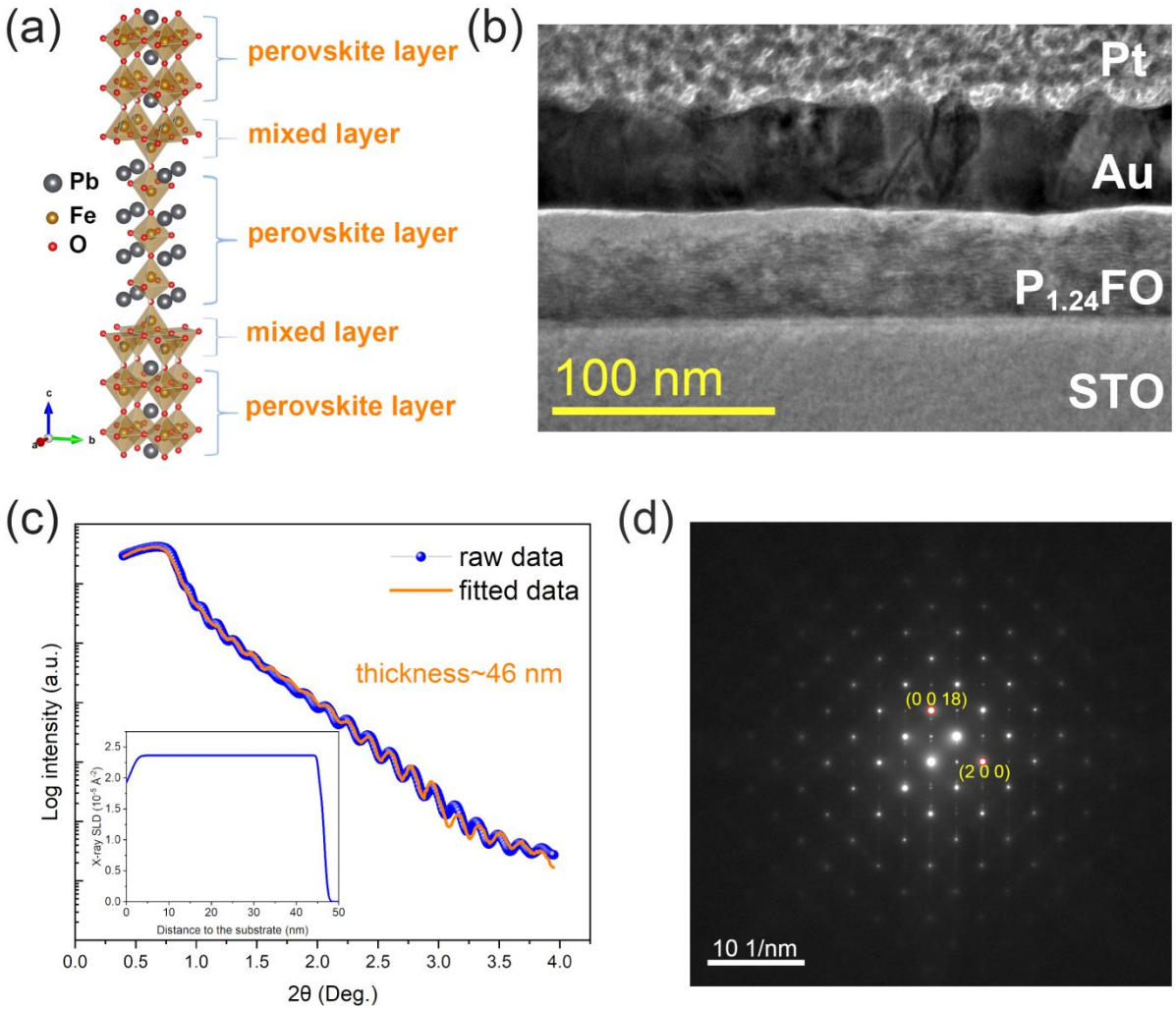

Figure S2. (a) The structural schematic diagram of $Pb_2Fe_2O_5$. (b) The low-magnification image shows the sharp interface in an extensive range. (c) The measured (blue block) and fitted (orange line) XRR curves of the $P_{1.24}FO$ film. Inset is the X-ray scattering length density (SLD) depth profile as a function of the distance from the STO substrate. The film thickness is about 46 nm, acquired from modelling the XRR pattern by using GenX. (d) The electron diffraction image demonstrates the excellent single crystallinity.

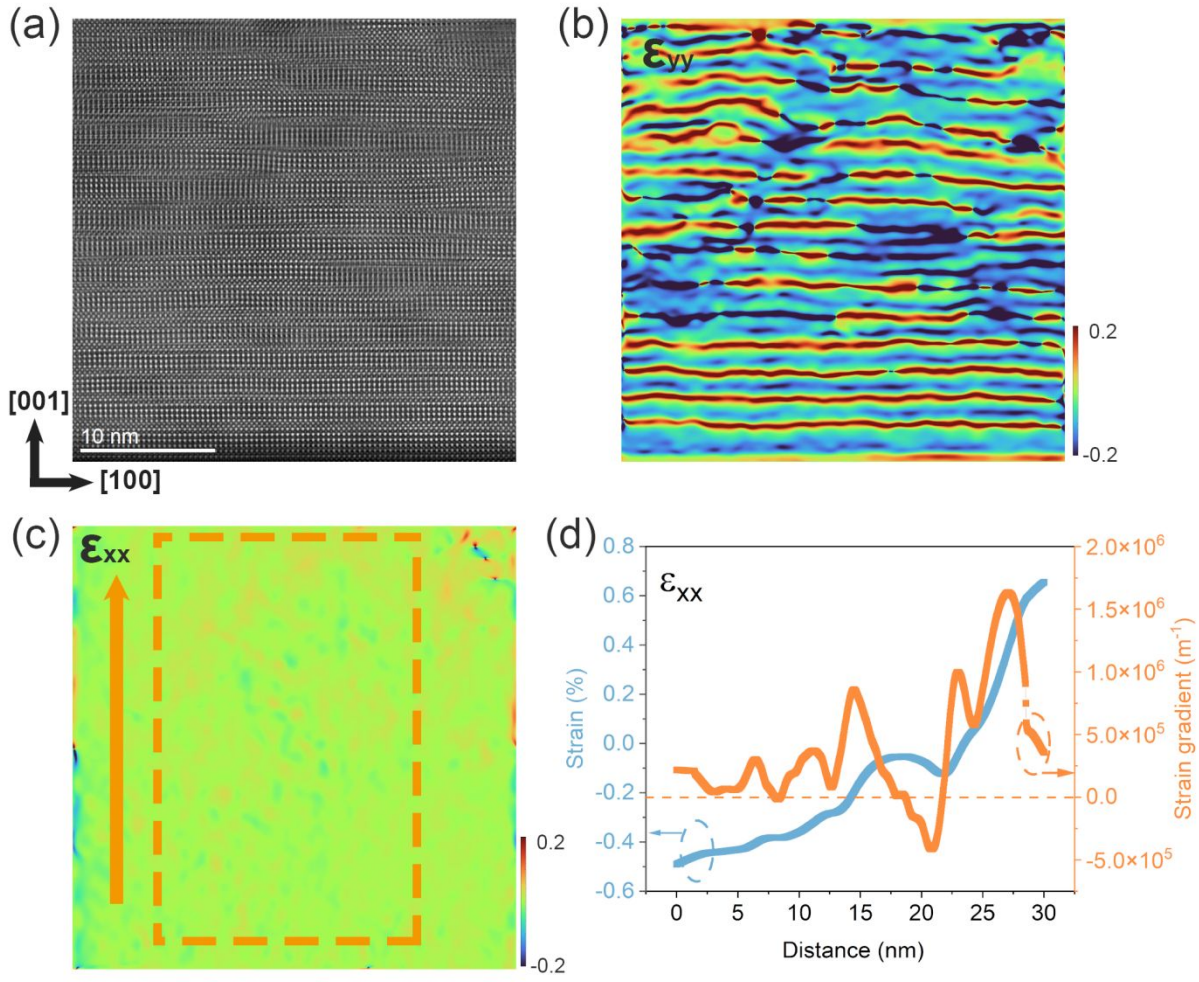

Figure S3. (a) STEM-HAADF image of $P_{1.24}FO$ film in an extensive range. (b) The out-of-plane strain ε_{yy} image of (a) by GPA. (c) The in-plane strain ε_{xx} image of (a) by GPA. (d) The in-plane strain gradient variation along [001] within the orange dashed box in (c).

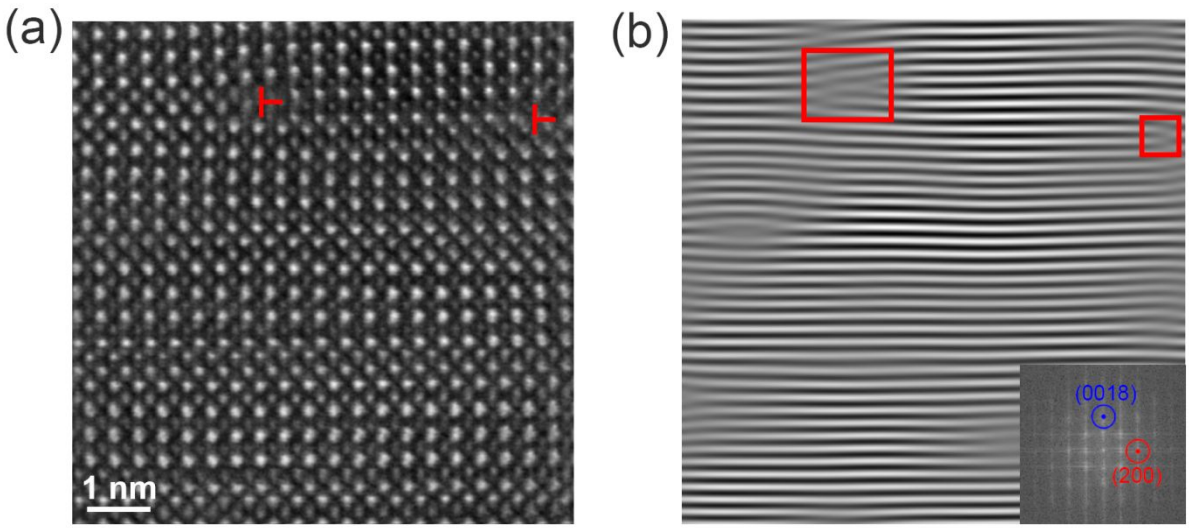

Figure S4. (a) The dislocations of $P_{1.24}FO$ film are shown by the HAADF image. (b) Inverse fast Fourier transformation (FFT) of (a). Two dislocations are highlighted by the red box.

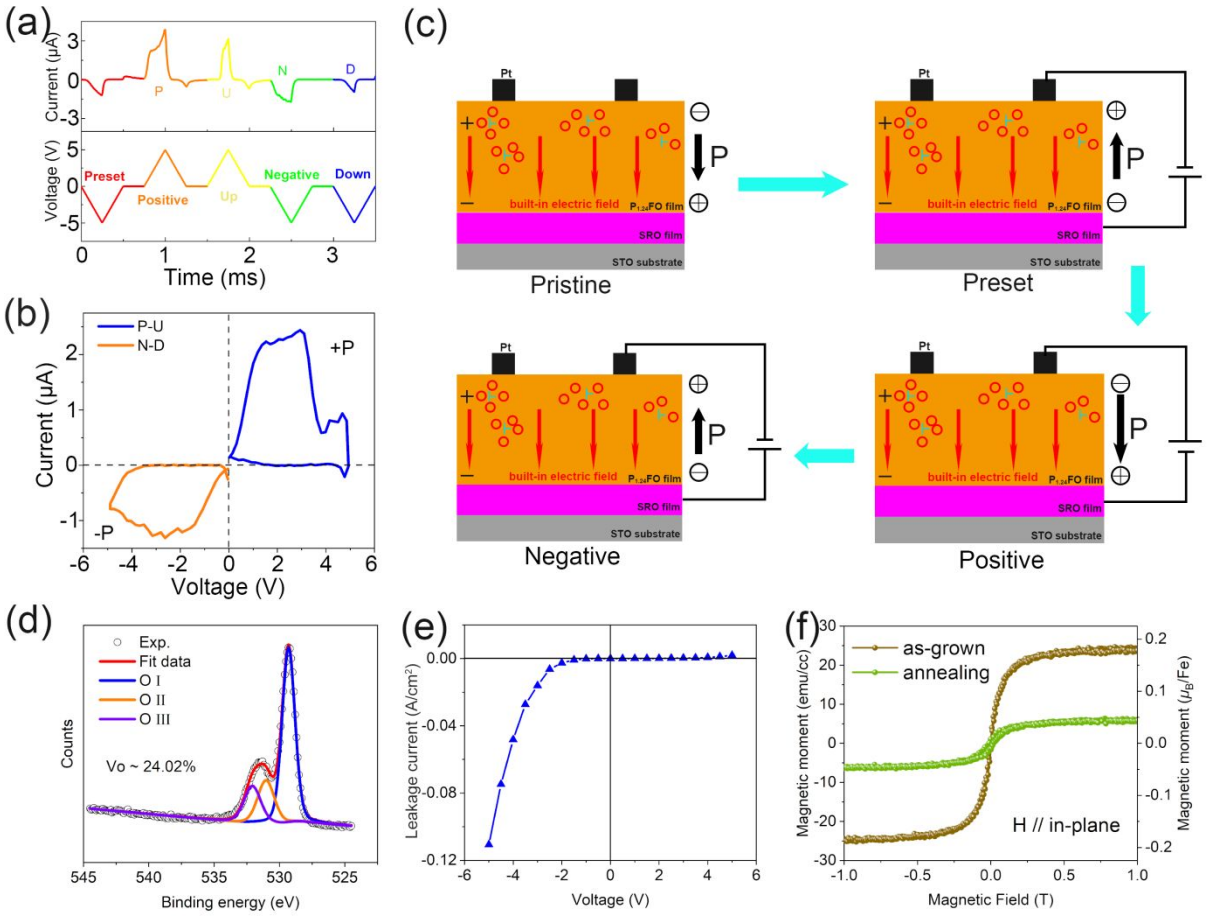

Figure S5. (a) Time-dependent triangular wave voltage (ranging from -5 V to +5 V, bottom) and displacement current (top) measured in PUND mode. (b) The polarization displacement current *vs*. voltage. (c) Schematic diagram of the influence of the built-in electric field on ferroelectric polarization switching, where red circles and black circles represent oxygen vacancies and polarization charges, respectively; red arrows and black arrows represent the direction of the built-in electric field and polarization, respectively. (d) Deconvolutions of O 1*s* XPS analyses of $P_{1.24}FO$ film by using the Lorentz-Gaussian model, where the experimental data, lattice oxygen (O_{I}), oxygen vacancy (O_{II}) and adsorbed oxygen (O_{III}) are represented by black circles, blue line, orange line and purple line. (e) The leakage current density of $P_{1.24}FO$ film between –5 V and +5 V. (f) The hysteresis loops of $P_{1.24}FO$ film before and after annealing.

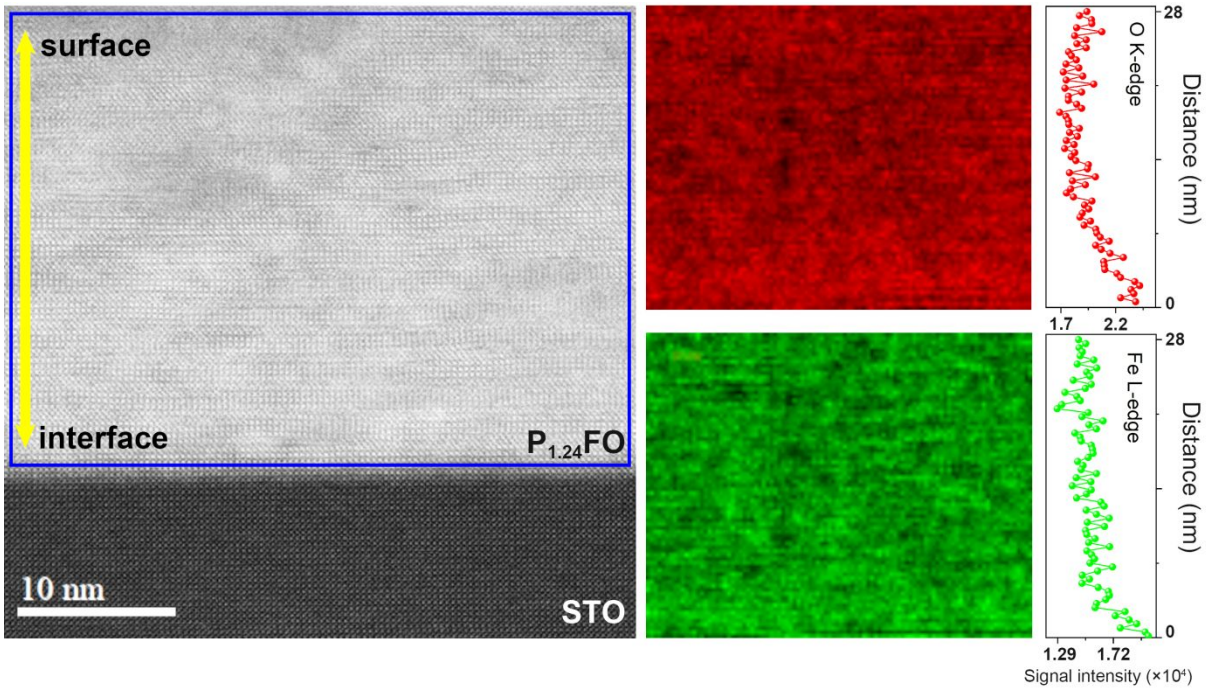

Figure S6. The STEM-EELS mapping of $P_{1.24}FO$ film for O *K*-edge and Fe *L*-edge.

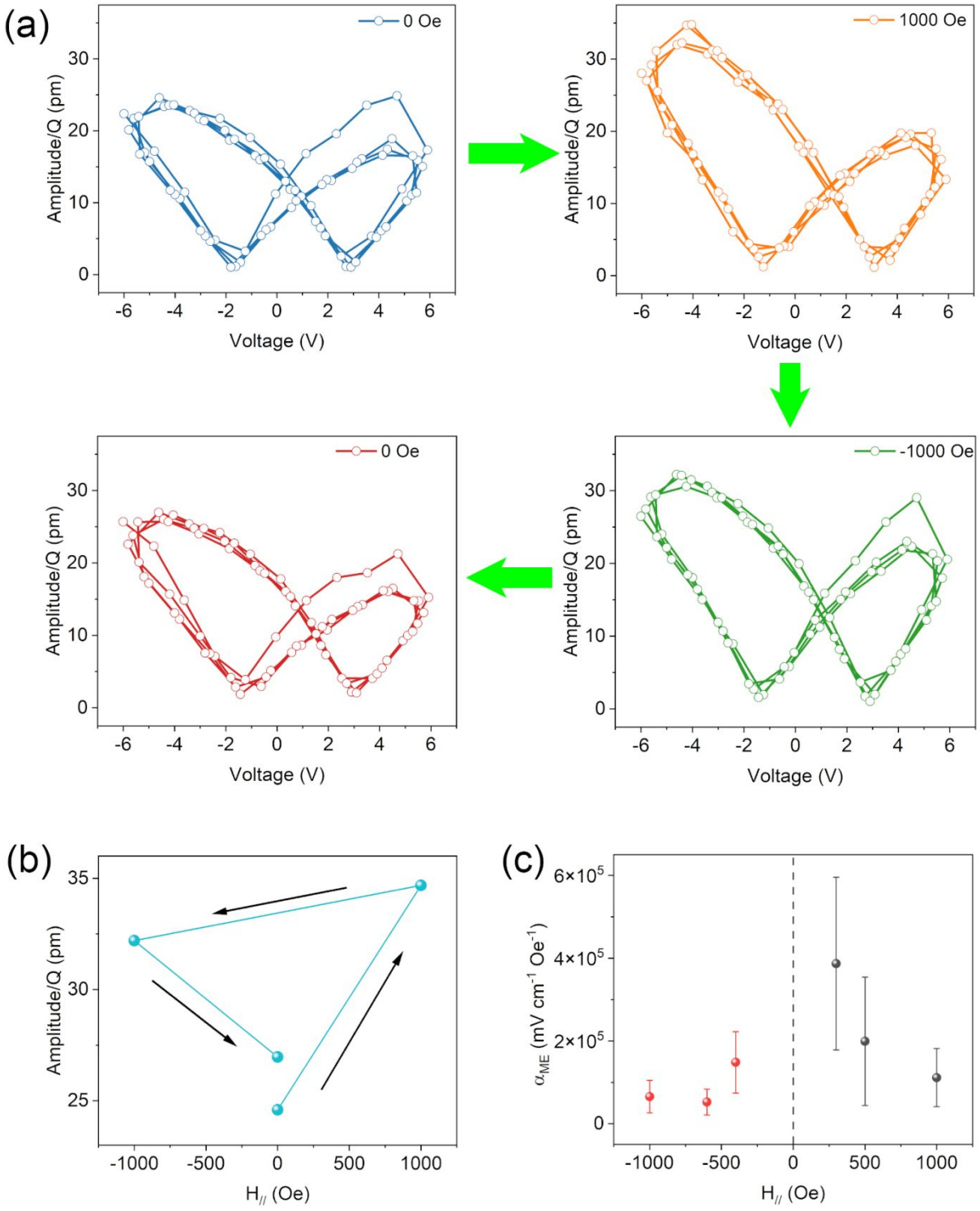

Figure S7. (a) The amplitude butterfly loops of $P_{1.24}FO$ film under various positive and negative parallel magnetic fields. (b) The amplitude *vs.* parallel magnetic field extracted from (a). (c) ME coupling coefficients under different magnetic fields.

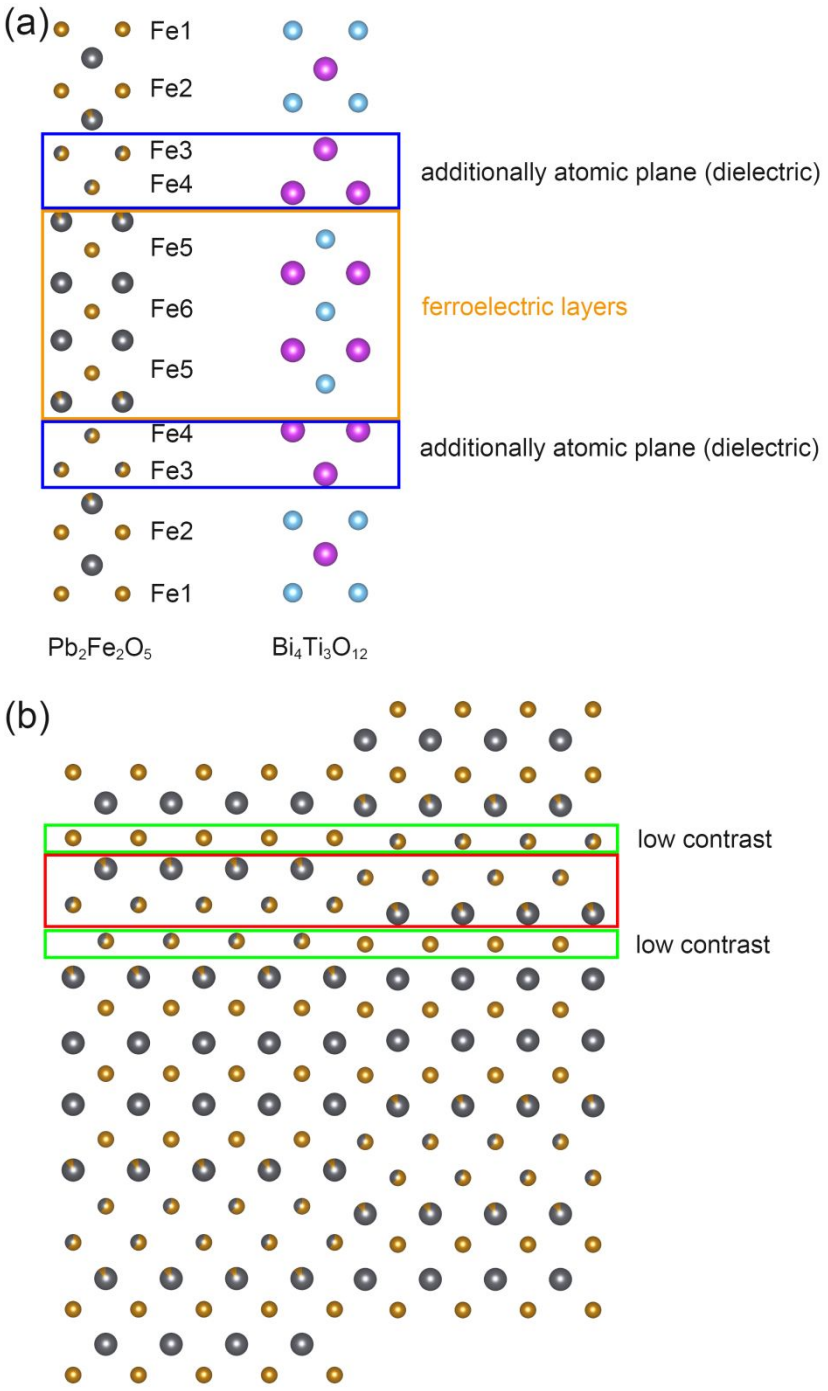

Figure S8. (a) The structural model of layered $Pb_2Fe_2O_5$ bulk and $Bi_4Ti_3O_{12}$ bulk, where the atomic distribution of the additional atomic planes in the two structures is different. (b) In the stacking fault model, the two sides of the mixed layer are low contrast. In contrast, in $P_{1.24}FO$ film, the two sides of the mixed layer are in high contrast, eliminating the possibility of stacking faults causing the locally ordered distribution of Pb/Fe atoms in mixed layers of $P_{1.24}FO$ films.

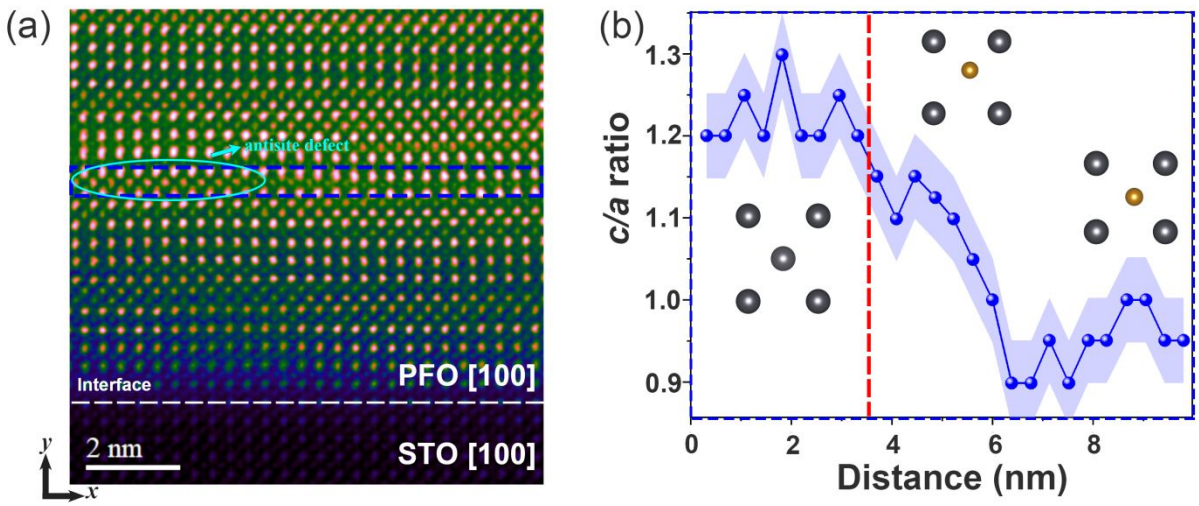

Figure S9. The influence of antisite defect on the c/a ratio of the perovskite layer. (a) The HAADF image of $P_{1.24}FO/STO$, where the cyan area represents the Pb_{Fe} antisite defect. (b) The variation of *c*/*a* ratio of the perovskite layer along x direction (dark blue dashed box in (a)).

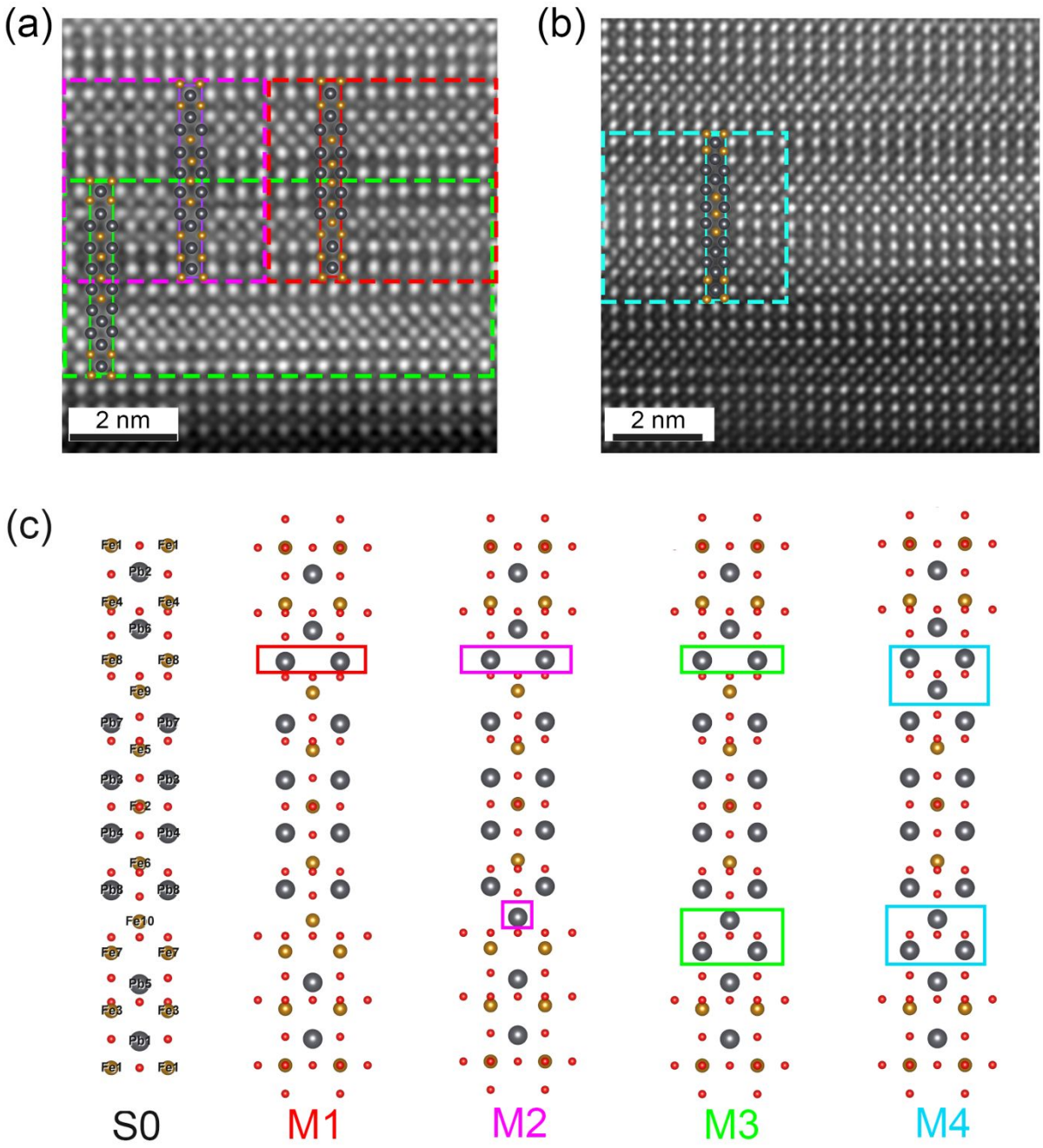

Figure S10. Model diagrams of reference structure and Pb replacing the different positions of Fe in the mixed layers (M1, M2, M3 and M4).

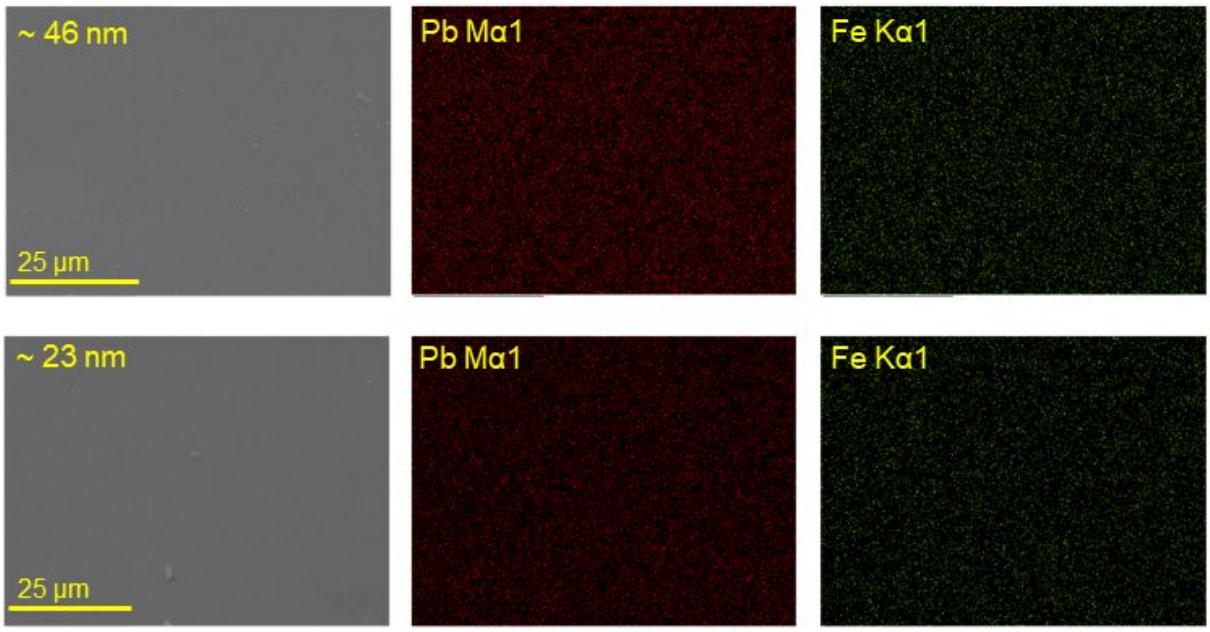

Figure S11. The EDS measurement of PFO film with different thicknesses.

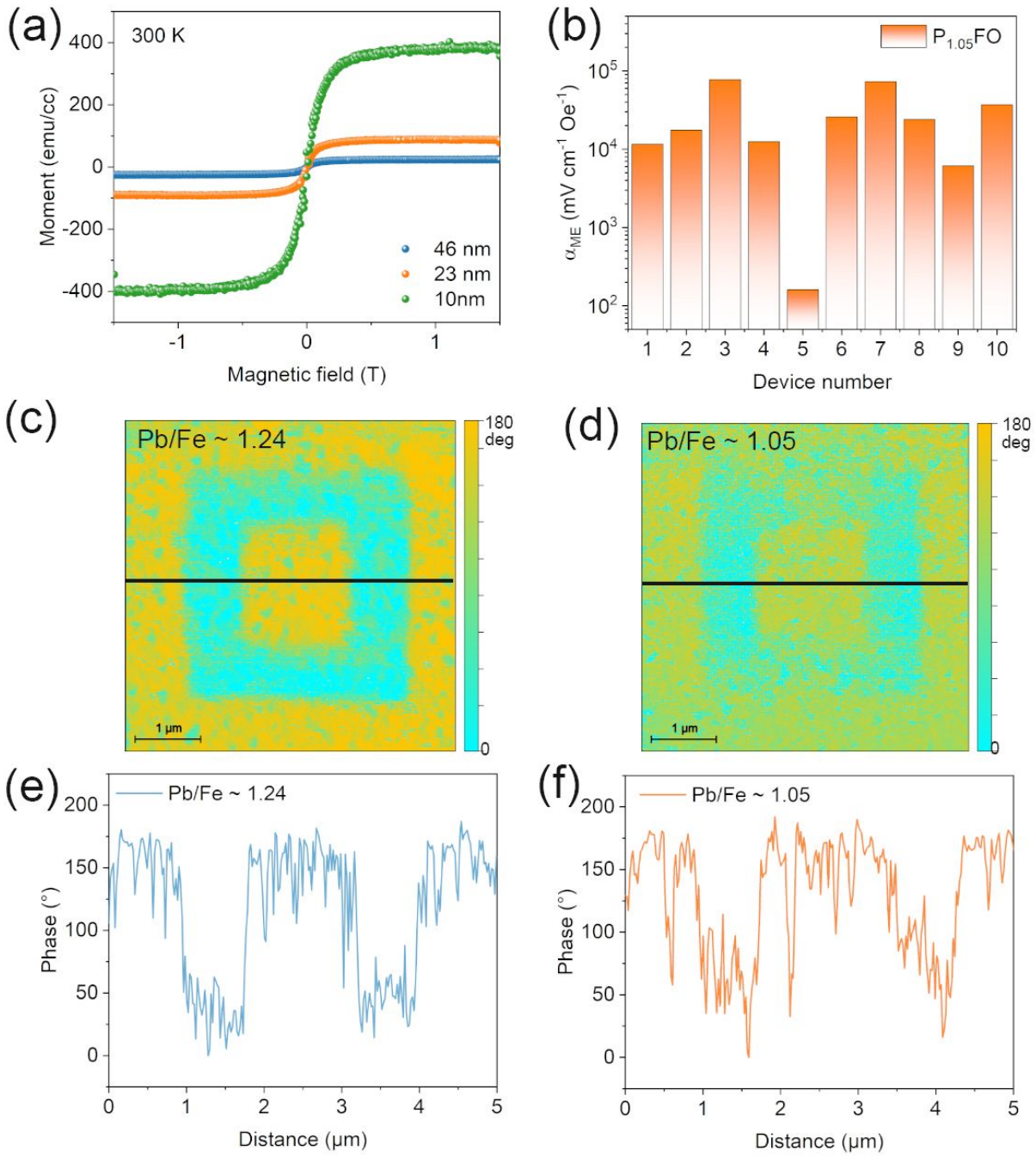

Figure S12. (a) The *M-H* hysteresis loops of films with different thicknesses. (b) The ME coupling coefficients at different areas of $P_{1.24}FO$ film (~ 92 nm) and $P_{1.05}FO$ film (~ 46 nm). (c) The PFM image of $P_{1.24}FO$ film and its phase-distance profile (e). (d) The PFM image of $P_{1.05}FO$ film and its phase-distance profile (f).

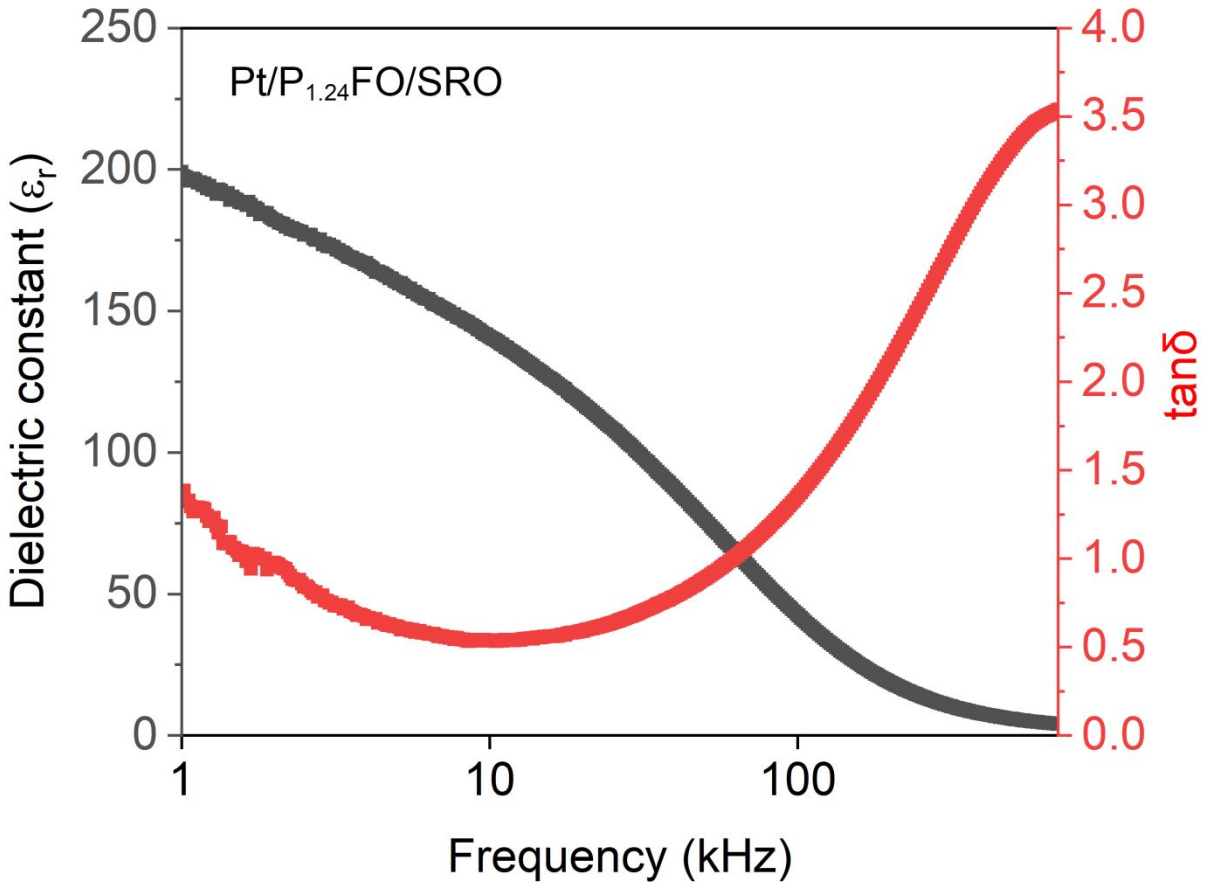

Figure S13. The variation of dielectric constant and loss with frequency in $P_{1.24}FO$ film.

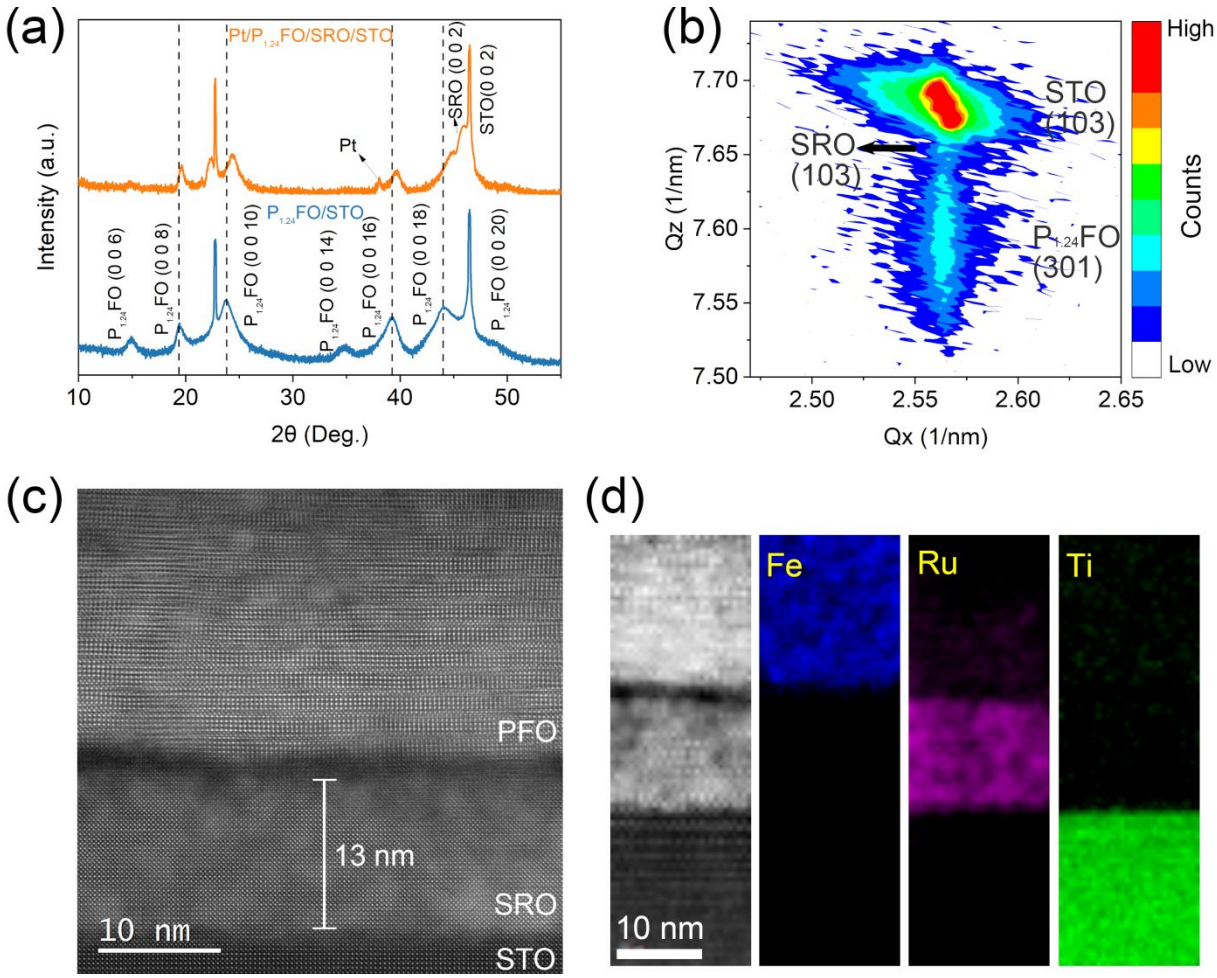

Figure S14. (a) XRD patterns of $P_{1.24}FO$/STO and $P_{1.24}FO$/SRO/STO. (b) RSM near the (103) spot of the STO substrate. (c) HAADF image of $P_{1.24}FO$/SRO/STO along STO [010] zone axis. (d) EELS mapping of $P_{1.24}FO$/SRO/STO.

Table S1. The lattice parameters and strain of $P_{1.24}FO$ films grown on STO and SRO, PFO bulk and STO substrate.

	In-plane		Out-of-plane	
	a (Å)	ε_x (%)	c (Å)	ε_y (%)
$P_{1.24}FO$ film (grown on STO)	3.905	0	36.48	1.3
$P_{1.24}FO$ film (grown on SRO)	3.905	0	36.34	0.9
PFO bulk[1]	3.905	-	36	-
STO substrate	3.905	-	3.905	-

Table S2. Total energy of Pb replacing Fe at different positions.

Configurations	Number of Pb replacing Fe	Energy (eV)	
$\mathbf{Pb_{Fe1}}$	1	3.56	Perovskite layers
$\mathbf{Pb_{Fe2}}$		2.88	
$\mathbf{Pb_{Fe3}}$		1.60	
$\mathbf{Pb_{Fe4}}$		0.44	
$\mathbf{Pb_{Fe5}}$		3.11	
$\mathbf{Pb_{Fe6}}$		1.14	
$\mathbf{Pb_{Fe7}}$		0.82	Mixed layers
$\mathbf{Pb_{Fe8}}$		0.44	
$\mathbf{Pb_{Fe9}}$		0	
$\mathbf{Pb_{Fe10}}$		1.72	
$\mathbf{Pb_{Fe8,9}}$	2	0	Mixed layers
$\mathbf{Pb_{Fe8,10}}$		0.04	
$\mathbf{Pb_{Fe4,8}}$		1.50	Mixed and Perovskite layers
$\mathbf{Pb_{Fe4,9}}$		1.13	
$\mathbf{Pb_{Fe6,8}}$		0.76	
$\mathbf{Pb_{Fe6,9}}$		0.69	
$\mathbf{Pb_{Fe7,8,9}}$	3	0	Mixed layers
$\mathbf{Pb_{Fe8,9,10}}$		0.30	
$\mathbf{Pb_{Fe1,8,9}}$		2.63	Mixed and Perovskite layers
$\mathbf{Pb_{Fe3,8,9}}$		0.33	
$\mathbf{Pb_{Fe4,8,9}}$		0.89	

Table S3. Structural relaxation optimization results for four competing structures.

Structures	Space group	Number of perovskite unit cells	Displacement of Fe ions (Å)		Net average displacement (Å/Fe)	c/a ratio of perovskite unit cells
M1	P4mm	7	Fe1	0.06	-0.02	0.90
			Fe2	-0.12		0.95
			Fe3	0.18		1.10
			Fe4	-0.30		1.15
			Fe5	0.08		1.00
			Fe6	-0.28		1.10
			Fe8	0.26		1.10
M2	P4mm	8	Fe1	0.06	0.17	0.90
			Fe2	0.22		1.00
			Fe3	0.14		1.02
			Fe4	-0.15		1.05
			Fe5	0.17		1.00
			Fe6	0.18		1.05
			Fe7	0.37		1.15
			Fe8	0.35		1.15
M3	P4mm	7	Fe1	-0.13	-0.05	0.90
			Fe2	-0.02		0.95
			Fe3	-0.03		1.08
			Fe4	-0.18		1.10
			Fe5	0.41		1.10
			Fe6	-0.22		0.98
			Fe7	-0.19		1.08
M4	I4/mmm	6	Fe1	0	0	0.90
			Fe2	0		0.90
			Fe3	0.15		0.92
			Fe4	-0.15		0.92
			Fe5	0.15		0.92
			Fe6	-0.15		0.92

Table S4. The relative content of Pb and Fe in PFO film with different thicknesses.

PFO film thickness (nm)	Pb (at%)	Fe (at%)	Pb/Fe ratio
46	2.19	1.77	1.24
23	1.07	0.93	1.05

References:

(1) Batuk, D.; Hadermann, J.; Abakumov, A.; Vranken, T.; Hardy, A.; Van Bael, M.; Van Tendeloo, G. Layered Perovskite-Like $Pb_2Fe_2O_5$ Structure as a Parent Matrix for the Nucleation and Growth of Crystallographic Shear Planes. *Inorg. Chem.* **2011**, *50* (11), 4978–4986. https://doi.org/10.1021/ic200211x.

(2) Yu, P.; Luo, W.; Yi, D.; Zhang, J. X.; Rossell, M. D.; Yang, C.-H.; You, L.; Singh-Bhalla, G.; Yang, S. Y.; He, Q.; Ramasse, Q. M.; Erni, R.; Martin, L. W.; Chu, Y. H.; Pantelides, S. T.; Pennycook, S. J.; Ramesh, R. Interface Control of Bulk Ferroelectric Polarization. *Proc. Natl. Acad. Sci. U.S.A.* **2012**, *109* (25), 9710–9715. https://doi.org/10.1073/pnas.1117990109.

(3) Huang, B.; Zhao, X.; Li, X.; Li, L.; Xie, Z.; Wang, D.; Feng, D.; Jiang, Y.; Liu, J.; Li, Y.; Yuan, G.; Han, Z.; Paudel, T. R.; Xing, G.; Hu, W.; Zhang, Z. Schottky Barrier Control of Self-Polarization for a Colossal Ferroelectric Resistive Switching. *ACS Nano* **2023**, *17* (13), 12347–12357. https://doi.org/10.1021/acsnano.3c01548.

(4) Cai, S.; Lun, Y.; Ji, D.; Lv, P.; Han, L.; Guo, C.; Zang, Y.; Gao, S.; Wei, Y.; Gu, M.; Zhang, C.; Gu, Z.; Wang, X.; Addiego, C.; Fang, D.; Nie, Y.; Hong, J.; Wang, P.; Pan, X. Enhanced Polarization and Abnormal Flexural Deformation in Bent Freestanding Perovskite Oxides. *Nat. Commun.* **2022**, *13* (1), 5116. https://doi.org/10.1038/s41467-022-32519-2.

(5) Nguyen, T. D.; Mao, S.; Yeh, Y.; Purohit, P. K.; McAlpine, M. C. Nanoscale Flexoelectricity. *Adv. Mater.* **2013**, *25* (7), 946–974. https://doi.org/10.1002/adma.201203852.

(6) Chen, C.; Liu, H.; Lai, Q.; Mao, X.; Fu, J.; Fu, Z.; Zeng, H. Large-Scale Domain Engineering in Two-Dimensional Ferroelectric $CuInP_2S_6$ via Giant Flexoelectric Effect. *Nano Lett.* **2022**, *22* (8), 3275–3282. https://doi.org/10.1021/acs.nanolett.2c00130.

(7) Ni, X.; Wong, Z. J.; Mrejen, M.; Wang, Y.; Zhang, X. An Ultrathin Invisibility Skin Cloak for Visible Light. *Science* **2015**, *349* (6254), 1310–1314. https://doi.org/10.1126/science.aac9411.

(8) Gao, R.; Reyes-Lillo, S. E.; Xu, R.; Dasgupta, A.; Dong, Y.; Dedon, L. R.; Kim, J.; Saremi, S.; Chen, Z.; Serrao, C. R.; Zhou, H.; Neaton, J. B.; Martin, L. W. Ferroelectricity in $Pb_{1+\delta}ZrO_3$ Thin Films. *Chem. Mater.* **2017**, *29* (15), 6544–6551. https://doi.org/10.1021/acs.chemmater.7b02506.

(9) Ning, S.; Kumar, A.; Klyukin, K.; Cho, E.; Kim, J. H.; Su, T.; Kim, H.-S.; LeBeau, J. M.; Yildiz, B.; Ross, C. A. An Antisite Defect Mechanism for Room Temperature Ferroelectricity in Orthoferrites. *Nat. Commun.* **2021**, *12* (1), 4298. https://doi.org/10.1038/s41467-021-24592-w.

(10) Lin, J. L.; Sun, Y.; He, R.; Li, Y.; Zhong, Z.; Gao, P.; Zhao, X.; Zhang, Z.; Wang, Z. J. Colossal Room-Temperature Ferroelectric Polarizations in $SrTiO_3/SrRuO_3$ Superlattices Induced by Oxygen Vacancies. *Nano Lett.* **2022**, *22* (17), 7104–7111. https://doi.org/10.1021/acs.nanolett.2c02175.

(11) Li, H.; Yang, Y.; Deng, S.; Zhang, L.; Cheng, S.; Guo, E.-J.; Zhu, T.; Wang, H.; Wang, J.; Wu, M.; Gao, P.; Xiang, H.; Xing, X.; Chen, J. Role of Oxygen Vacancies in Colossal Polarization in $SmFeO_{3-\delta}$ Thin Films. *Sci. Adv.* **2022**, *8* (13), eabm8550. https://doi.org/10.1126/sciadv.abm8550.

(12) Zhou, C.; Ma, L.; Feng, Y.; Kuo, C.-Y.; Ku, Y.-C.; Liu, C.-E.; Cheng, X.; Li, J.; Si, Y.; Huang, H.; Huang, Y.; Zhao, H.; Chang, C.-F.; Das, S.; Liu, S.; Chen, Z. Enhanced Polarization Switching Characteristics of HfO_2 Ultrathin Films via Acceptor-Donor Co-Doping. *Nat. Commun.* **2024**, *15* (1),

2893. https://doi.org/10.1038/s41467-024-47194-8.

(13) Yang, Y.; Wu, M.; Zheng, X.; Zheng, C.; Xu, J.; Xu, Z.; Li, X.; Lou, X.; Wu, D.; Liu, X.; Pennycook, S. J.; Wen, Z. Atomic-Scale Fatigue Mechanism of Ferroelectric Tunnel Junctions. *Sci. Adv.* **2021**, *7* (48), eabh2716. https://doi.org/10.1126/sciadv.abh2716.